Insights into the Effect of Heat Treatment and Carbon Coating on the Electrochemical Behaviors of SiO Anodes for Li-ion Batteries

Shuai Xu, Xiaodong Hou, Dongniu Wang, Lucia Zuin, Jigang Zhou, Yong Hou, and Michael Mann*

Shuai Xu, Xiaodong Hou, Yong Hou, and Michael Mann

Institute for Energy Studies, University of North Dakota, Grand Forks, ND, 58202, United States

*E-mail: xiaodong.hou@und.edu

Dongniu Wang, Lucia Zuin, Jigang Zhou

Canadian Light Source Inc., Saskatoon, S7N 2V3, Canada

Keywords: silicon monoxide, heat treatment, disproportionation, carbon coating, lithium-ion batteries

The use of silicon monoxide (SiO) as an anode material has attracted significant interest due to its high capacity and long cycling life. Many promising approaches, including structural design and carbon coating at high temperatures, effectively improve its intrinsic low electrical conductivity and poor coulombic efficiency. However, the "heat-treatment process - composition and microstructure - electrochemical properties" relationship of the SiO anode is not fundamentally understood. Here the structure and composition evolution in amorphous SiO and graphene-coated SiO is investigated using different heat treatment conditions. The X-ray Absorption Near-Edge Structure (XANES) techniques are also employed to analyze the surface and bulk composition change during the initial lithiation process, supplemented by physical or chemical characterization and electrochemical testing. The results reveal the structural transition of SiO during heat treatment, from amorphous to disproportionated hierarchical structure, where the as-formed dielectric exterior SiO_2 shell and interior SiO_2 matrix severely polarizes electrodes, hindering the lithiation process. Carbon coating on SiO effectively restricts the growth of the SiO_2 shell and facilitates charge transfer, leading to improved electrochemical performance. Eventually, a schematic model is proposed to reveal the relationship between the treatments, the resultant structural evolutions, and corresponding electrochemical behaviors.

This is the author manuscript accepted for publication and has undergone full peer review but has not been through the copyediting, typesetting, pagination and proofreading process, which may lead to differences between this version and the Version of Record. Please cite this article as doi: 10.1002/aenm.202200127.

1. Introduction

Silicon-based materials (e,g., Si and SiO) are expected to replace graphite (372 mAh g^{-1}) to increase the energy densities of Li-ion batteries (LIBs) owing to their high specific capacity (4200 mAh g^{-1} for Si).[1] However, Si's high capacity is offset by its significant volume expansion (~ 400%) during lithiation, which pulverizes its particles, causing the Si particles to lose contact with electrodes.[2] The side reactions between Si and electrolytes form the solid-electrolyte interface (SEI), which is unstable during lithiation/delithiation cycles and consumes the electrolyte continuously, resulting in a thick SEI and deteriorated Li^+ transport. These problems contribute to low cycling efficiency and rapid capacity loss.[2a, 3]

Silicon monoxide (SiO) possesses a compromised theoretical capacity of ~ 2400 mAh g^{-1},[4] with a much smaller volume expansion (~ 200%), making it more practical for LIBs when compared to Si alone;[5] however, an accurate structural model of the SiO materials remains controversial after decades of experimental and theoretical efforts.[6] Two structural models, the random-mixture (RM) and random-bonding (RB) were proposed to address SiO's composition and valence distribution.[7] The RM model posits that SiO exists as a stoichiometric mixture of amorphous SiO_2 and amorphous Si,[8] while the RB model posits that silicon exists with the valence of 0 to+4 randomly connecting the oxygen atoms.[9] A recent study indicates that Si nanoclusters (Si^0) are surrounded by an amorphous SiO_2 matrix (Si^{4+}). Some silicon exists with valences of +1, +2, and +3 in their interfacial regions.[10] SiO's unique composition and structure allow it to deliver greater cycling performance than Si anodes. The reason for that is the reaction between amorphous SiO_2 matrix and Li-ions in the initial lithiation process, forming irreversible Li_2O and Li silicates. Both can act as a buffer phase that effectively alleviates the significant volume change of the Si nanoclusters.[11] However, the irreversible reactions also account for a major capacity loss, corresponding to a low initial coulombic efficiency (ICE).[12] As a result, SiO anodes show faster capacity failure than the commercial graphite anodes, though much slower than Si anode. Other failure mechanisms include the intrinsic inferior electrical conductivity, the electrical isolation effect caused by volume changes during cycling,[13] and considerable side reactions with electrolytes.[14] Mitigation of those failure mechanisms is crucial for the commercialization of SiO in LIBs.[15]

Some approaches, including conductive coating,[16] structural design,[17] and chemical etching,[18] have been performed to improve the electrochemical performance of SiO anode. These approaches usually involve a heat treatment process to calcinate the SiO-related precursors. However, up to date the impact of heat treatments on the SiO microstructure is not fully studied probably due to its thermal instability. Heat treatment can expedite the disproportionation reaction of SiO:[19]

$$2SiO \rightarrow Si + SiO_2$$

Higher temperatures (>800 °C) and longer heating times can accelerate this reaction and promote the Si and SiO_2 phase separation, which is indicated by the increased nanocluster size and crystallinity of the Si phase.[19] [20] Intensive studies on SiO have demonstrated that the Si and SiO_2 phase growth and separation can significantly impact its electrochemical performance.[5a, 20a] For instance, the electrical resistance of the disproportionated SiO materials (D-SiO) increases as the dielectric SiO_2 matrix phase becomes denser.[21] As a result, D-SiO becomes inert during lithiation.[20a] However, there are still some unsolved questions on this matter. *1)* How does the surface composition and structure of the SiO anode particles change during heat treatment? Reports were focused on its bulk properties instead of the surface, which plays a crucial role in the electrochemical behaviors, including SEI formation, initial lithiation, and charge transfer resistance. The overpotential that appeared in the initial lithiation of D-SiO has not been thoroughly investigated yet.[20a, 22] *2)* What is the formation mechanism of "Si nanowires" often observed during heat treatment?[23] It reports "Si nanowires" formed on the surface of SiO particles when heated from 900-1100 °C, and these nanowires were deemed conducive to the electrochemical performance of a SiO-based anode. However, the report failed to provide a detailed analysis of its formation mechanism, synthetic atmosphere, distribution, and content.[23b] *3)* How does carbon coating impact the composition and microstructure evolution of SiO materials during heat treatment? *4)* How does the composition and microstructure evolution impact the electrochemical performance of SiO anodes? Several researchers have investigated the impact of heat treatment on ICE and the cycling life of SiO anodes, but their results are often contradictory.[22, 24]

To shed a light on those fundamental questions, herein we present a systematic study on this matter. We start with investigating the effects of heat treatment and carbon coating processes on the morphology, microstructure, and chemical composition of SiO by using a series of microanalysis techniques, such as SEM, Raman, and XRD. Our work is focused on analyzing the dynamic evolution of the Si and SiO_2 phases during the process. We further analyze and compare three anode particles, namely pristine SiO (P-SiO), D-SiO, and carbon-coated D-SiO (D-SiO@G), before and after cycling by XANES technique (Li-K and Si L-edge), supplemented with battery cycling life and electrochemical impedance spectroscopy (EIS) testing. At last, we propose a SiO structural model to illustrate the relationships of "synthetic processes-microstructure-electrochemical behaviors".

2. Results and Discussion

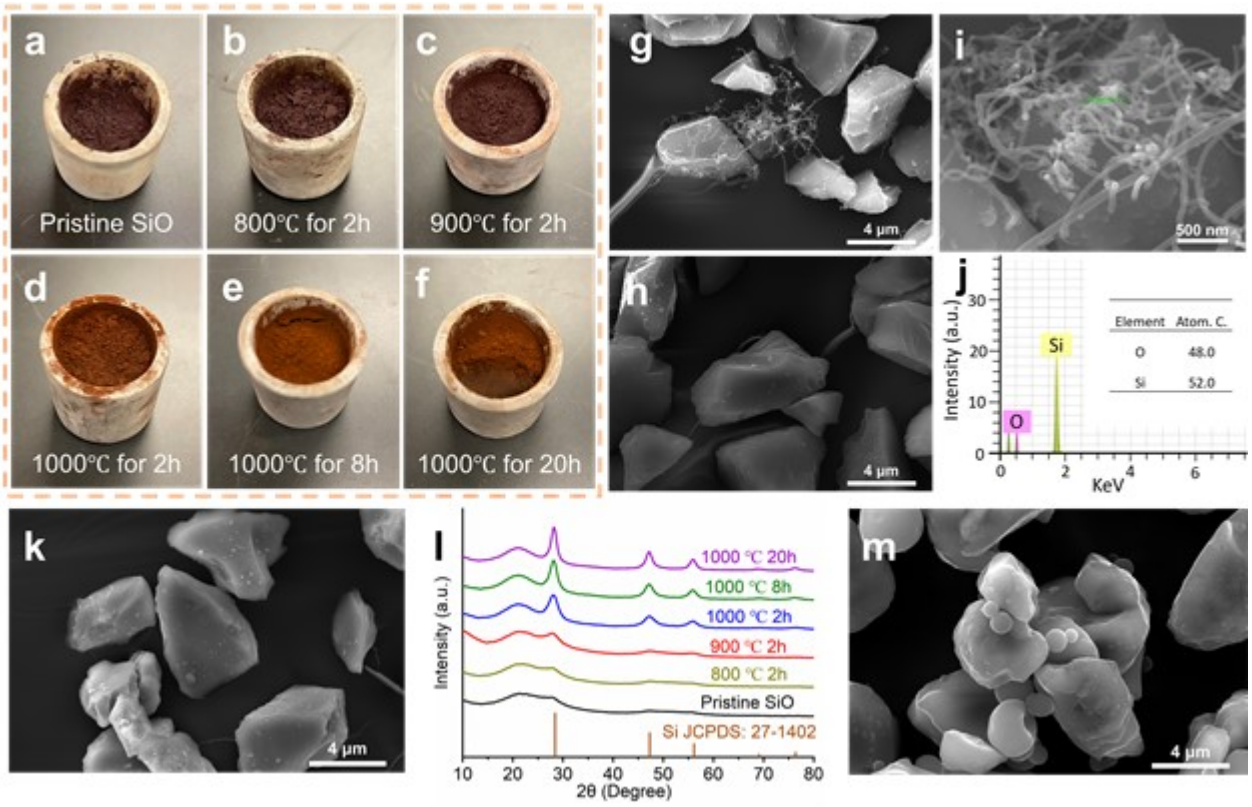

Figure 1. a-f) Photos of crucibles with SiO powder after heat treatments. SEM images of g) The D-SiO particles in the top red-brown substance (TRS), h) D-SiO particles under the TRS. i) EDX analysis spot of the Si nanowires, and j) Corresponding elemental content. k) SEM image of the pristine SiO (P-SiO). l) XRD patterns of the P-SiO and D-SiO samples. m) SEM image of the D-SiO@G particles.

Figure 1a-f depicts the photos of the pristine SiO (P-SiO) and D-SiO samples after heat treatments under a reducing atmosphere. The pristine P-SiO powder (Figure 1a) is brownish-black, similar to the appearance of the D-SiO samples prepared at lower temperatures (Figure 1b and 1c). The D-SiO powder in the crucibles is covered with a thin topping of a reddish-brown substance (TRS) when heated at 1 000 °C for 2 h and above (Figure 1d-1f), as indicated by the cross-section of the D-SiO-1000-20 powder (Figure 1f). The TRS accounts for about 1/25 (1000 °C for 2h) to 1/9 (1000 °C for 20h) in weight of the D-SiO powder (Figure S1). SEM inspection reveals that some nanowires (Figure 1g) are attached to D-SiO particles in the TRS layer, while the bulk of the D-SiO powder under the TRS is composed of D-SiO particles (Figure 1h) that are identical to the P-SiO particles (Figure 1k) with no interparticle nanowires. The EDX elemental analysis (Figure 1j) reveals that the nanowires consist of silicon and oxygen with atomic contents of 48.0 and 52.0% (Figure 1j), respectively. The atomic ratio of silicon to oxygen (~ 1:1) indicates that the so-called "Si nanowires" are primarily SiO, formed by the sublimation of SiO and the subsequent deposition of SiO vapor under high temperatures. These Si nanowires should have a crystalline silicon core and an amorphous SiO_2 sheath structure, as

indicated by previous reports.[25] The electrochemical improvements, if any, by the "Si nanowires" would be restricted for their insulating structure (dielectric SiO_2 sheath), small quantity, and localized distribution. It is worth noting that while under ultra-pure argon, which is one of the most widely-used atmospheres in research, a topping of white (instead of reddish-brown) nanowires in the TRS layer was observed. The white nanowires are composed of SiO_2 (Figure S2). Therefore we suspect the Si nanowires were oxidized by the trace oxygen in the high purity argon, which indicates the Si nanowires are extremely reactive at a high temperature. After the topping was removed, all the following characterizations were focused on the bottom part. The color of the D-SiO powder (Figure S3) becomes lighter with an increase of heating temperature and time, from the brownish-black similar to the P-SiO to brown when heated at 1000 °C for 20 h. This observation implies that a layer of the lighter color substance is likely enriched on the SiO particle surface. During the high-temperature treatment, the SiO vapor consisting of $(SiO)_n$ ($n \geq 1$) clusters would also deposit onto its surrounding D-SiO surfaces in addition to the formation of Si nanowires. Higher binding energy and lower surface strain are the driving forces of a stable configuration as calculated by the density-functional theory, which makes it energetically favorable for oxygen atoms to migrate from the core to surface, causing the structural transition:[18a, 26] An exterior SiO_2 shell forms on the surface of D-SiO particles, while the Si phase remains in the core, making the color of D-SiO powder lighter.

Another consequence of the heat treatment process is the evolution of the XRD patterns (Figure 1l). P-SiO exhibits an XRD pattern with a bump peak (15-30°). D-SiO-800-2 shows a similar XRD pattern as P-SiO, indicating that no apparent disproportionation reaction happens when heated at 800 °C for 2 h. Several peaks belonging to crystalline Si appear, become sharper and more intense as the temperature and heating time increase, while a broad peak (18 – 25°) attributed to amorphous SiO_2 is also separated from the SiO bump peak.[27]

The effect of the carbon coating on the SiO morphology evolution during the heat treatment process was also investigated. We used humic acid as the carbon source to create a conductive and resilient nano-graphene coating during the heat treatment process.[28] The synthesized D-SiO@G composites (Figure 1m) possess a similar particle size to P-SiO but with a rounded-edge shape because of the graphene coating. Importantly, no Si nanowire is found from the powder. The D-SiO@G particles etched with a 5% HF solution for 3 h (Figure S4) exhibit a thin and intact graphene coating, encapsulating the residual unetched D-SiO particles. The coating accounts for 9.1 wt% of the D-SiO@G and does not change the XRD patterns (Figure S5) compared to the D-SiO materials.

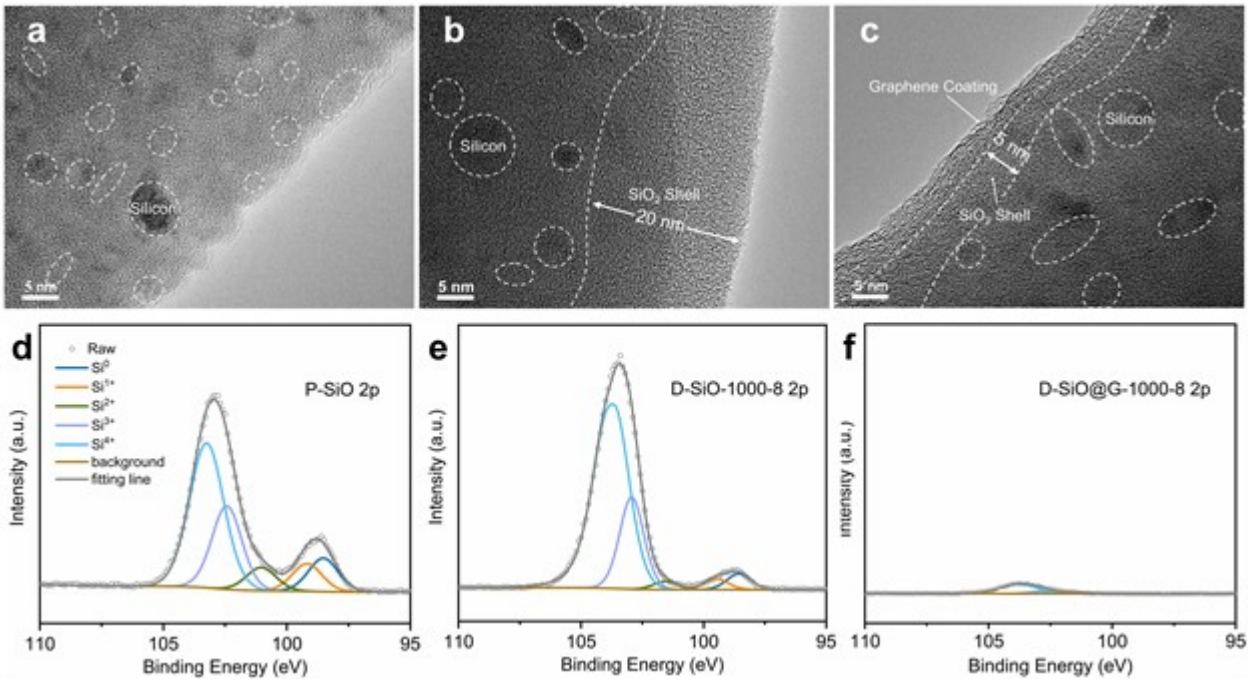

Figure 2. TEM images of a) P-SiO, b) D-SiO-1000-8, and c) D-SiO@G-1000-8. XPS spectra of Si 2p and their corresponding fitting peaks for d) P-SiO, e) D-SiO-1000-8, and f) D-SiO@G-1000-8.

High-resolution transmission electron microscopy (HRTEM) was performed to inspect the SiO's surface composition and microstructure changes during the heat treatment and graphene coating process. The observable lattice fringes belonging to Si nanoclusters are enclosed by the amorphous matrix, represented by white dashed circles in **Figures 2**a, b, and c. The HRTEM image of P-SiO (Figure 2a) indicates a swarm of Si nanoclusters a few nanometers in size randomly distributed in the amorphous SiO_2 matrix in the radial direction of the particle.[10] The HRTEM image of a D-SiO-1000-8 particle (Figure 2b) indicates that no Si nanoclusters can be found near the particle surface except for a thick amorphous SiO_2 shell (~ 20 nm) because of heat treatment. The Si nanoclusters are fewer but larger in size compared to P-SiO.[19, 24a] The HRTEM image of a D-SiO@G-1000-8 particle (Figure 2c) reveals the Si nanoclusters similar in size to D-SiO-1000-8, however, possess a much thinner amorphous SiO_2 shell (5 nm). The surface difference can be attributed to the intact graphene coating, which limits the sublimation and subsequent deposition of SiO and hinders oxygen migration from the core to the surface effectively, resulting in a thinner SiO_2 shell and the absence of Si nanowires in all carbon-coated samples. The TEM observations are also supported by X-ray photoelectron spectroscopy (XPS) results. The Si 2p peaks in all P-SiO spectra (Figure 2d), D-SiO-1000-8 (Figure 2e), and D-SiO@G-1000-8 (Figure 2f) can be fitted with five subpeaks corresponding to Si^0 (Si nanocluster), Si^{1+}, Si^{2+}, Si^{3+}, and Si^{4+} (SiO_2 matrix). The considerable Si and SiO_2 subpeaks in the P-SiO spectrum indicate prevalent Si nanoclusters and SiO_2 phases on the P-SiO particle surface,

which agree well with the TEM results. Intermediate valence (Si^{1+}, Si^{2+}, Si^{3+}) subpeaks experience considerable shrink from P-SiO to D-SiO-1000-8 due to the heat treatment process, since these valences disproportionate into Si^0 and Si^{4+}, forming larger Si nanoclusters and denser SiO_2 matrices; however, the Si^0 subpeak in D-SiO-1000-8 does not increase accordingly with the Si^{4+} peak but suffers significant reduction, which should be attributed to the cover of the exterior SiO_2 shell since the XPS only has a detective depth of a few nanometers for solid materials. The intact graphene coating of the D-SiO@G-1000-8 composite (Figure 2f) leads to a very weak Si 2p peak, in which Si^{4+} subpeak dominates, demonstrating the existence of the SiO_2 shell beneath the graphene coating.

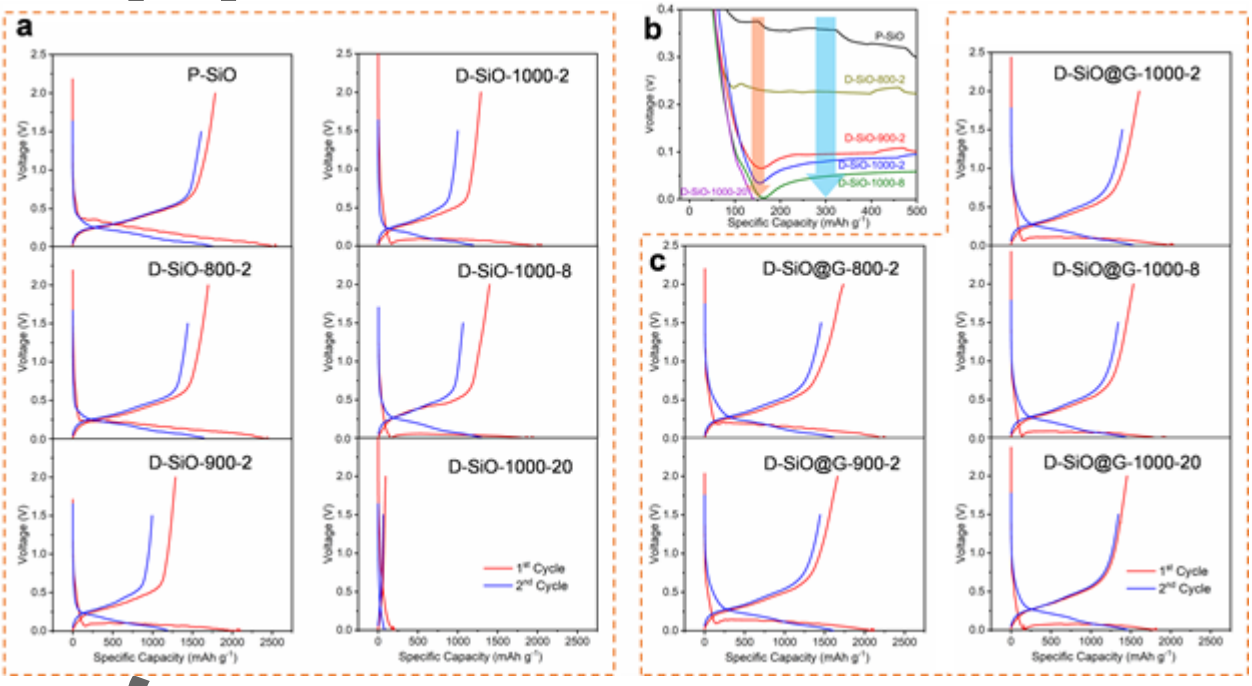

Figure 3. a) First and second charge-discharge curves of SiO after different heat treatments, and b) the overpotential of SiO samples. c) First and second charge-discharge curves of D-SiO@G.

We used half coin-cell testing to further investigate the effect of the heat treatment and carbon coating process on the SiO electrochemical behavior. **Figure 3**a illustrates the charge-discharge profiles of the first and second cycles of the P-SiO and D-SiO electrodes. P-SiO delivers the highest discharge capacity of 2564.8 mAh g^{-1} (**Table 1**) at a current density of 50 mA g^{-1}. D-SiO-800-2 delivers a capacity (2461.2 mAh g^{-1}) close to P-SiO since the heat treatment at 800°C for 2 h cannot make substantial changes to P-SiO. The initial discharge capacity decreases with an increase in temperature and heating time, accompanied by a decline in the discharge plateau potential, indicating that the overpotential of the electrodes increases drastically.[22] Figure 3b specifically depicts the overpotential evolution of all SiO samples. As lithiation begins, the max-overpotential point appears at the incipient stage of lithiation, at approximately 150 mAh g^{-1}. Higher heating

temperatures and longer heating times facilitate the formation of a thicker and denser SiO_2 shell, making it more resistant to electrochemical reactions.[21, 29] The shell with high electrical resistance and low Li^+ transport acts as a barrier, preventing the migration of Li-ions through the surface of the particles, causing the maximum resistance overpotential (orange arrow, Figure 3b). When the heat treatment is performed at 1000 °C for 20 h, the exterior SiO_2 shell is thick enough to completely prevent Li-ions from passing through, making the lithiation potential drop to 0 V versus the counter electrode (lithium metal), which indicates that Li-ions begin to deposit on the surface of the D-SiO particles, resulting in the capacity dive of D-SiO-1000-20. With lower heating temperatures or less heating times, Li-ions can pass through the barrier and react with Si nanoclusters inside the D-SiO particles, releasing more capacity (> 150 mAh g^{-1}, Figure 3b). The following lithiation process is also accompanied by the drop of the discharge plateau potential (blue arrow, Figure 3b), from 0.35 V for P-SiO to 0.07 V for D-SiO-1000-8 at the capacity of ~300 mAh g^{-1}, indicating that the amorphous interior SiO_2 matrix also becomes denser and more inert at high temperatures, causing a new resistance overpotential. Another valuable finding was that once Li-ions react with the SiO_2 shells and SiO_2 matrix, forming irreversible Li_2O and Li silicates, which are conducive to charge transfer and act as the access for Li^+ transport in the following cycles.[11] As a result, no resistance overpotential was observed since the second cycle of all samples (Figures 3a and 3c).

Table 1. Initial Discharge Capacity and ICE for P-SiO, D-SiO, and D-SiO@G samples.

SiO samples	Initial Cycle			D-SiO@G samples	Initial Cycle		
	Discharge (mAh g^{-1})	Charge (mAh g^{-1})	Efficiency (%)		Discharge (mAh g^{-1})	Charge (mAh g^{-1})	Efficiency (%)
P-SiO	2564.8	1709.3	69.8				
D-SiO-800-2	2461.2	1697.4	69.0	D-SiO@G-800-2	2264.4	1733.1	76.5
D-SiO-900-2	2107.9	1287.9	61.1	D-SiO@G-900-2	2124.2	1662.6	78.3
D-SiO-1000-2	1992.1	1204.2	60.4	D-SiO@G-1000-2	2044.0	1604.0	78.5
D-SiO-1000-8	1968.9	1395.0	70.9	D-SiO@G-1000-8	1942.8	1533.4	78.9
D-SiO-1000-20	207.9	93.9	45.2	D-SiO@G-1000-20	1831.1	1452.8	79.3

Figure 3c depicts the effect of graphene coating on the charge-discharge behaviors of the D-SiO samples. D-SiO@G samples treated at higher temperatures and longer times also present a decrease in initial discharge capacity, which is similar to the P-SiO and D-SiO samples; however, the sample D-SiO@G-1000-20 could overcome the overpotential barrier and deliver a considerable discharge capacity (1831.1 mAh g^{-1}), while its uncoated counterpart D-SiO-1000-20 could not. This difference should be attributed to the graphene coating that favors thinner SiO_2 shells and makes the D-SiO

particles more conductive, which alleviates the overpotential and facilitates charge transfer.[16a, 30] The graphene coating also significantly increases the ICE, as depicted in Table 1: D-SiO-800-2 has an ICE of only 69.0%, while the ICE of D-SiO@G-800-2 significantly increased to 76.5%. With the increase in heating temperature and time, the ICE further increases to 79.3% for D-SiO@G-1000-20. Two reasons for that are: 1) the graphene coating prevents the side reactions between the electrolyte and SiO materials, limiting the growth of the SEI film and leaving more Li-ions reversible, and 2) a higher temperature and longer heating time make the SiO_2 domains denser and more electrical resistant, limiting the formation of Li silicate, a well-known low Coulombic efficiency byproduct[31].

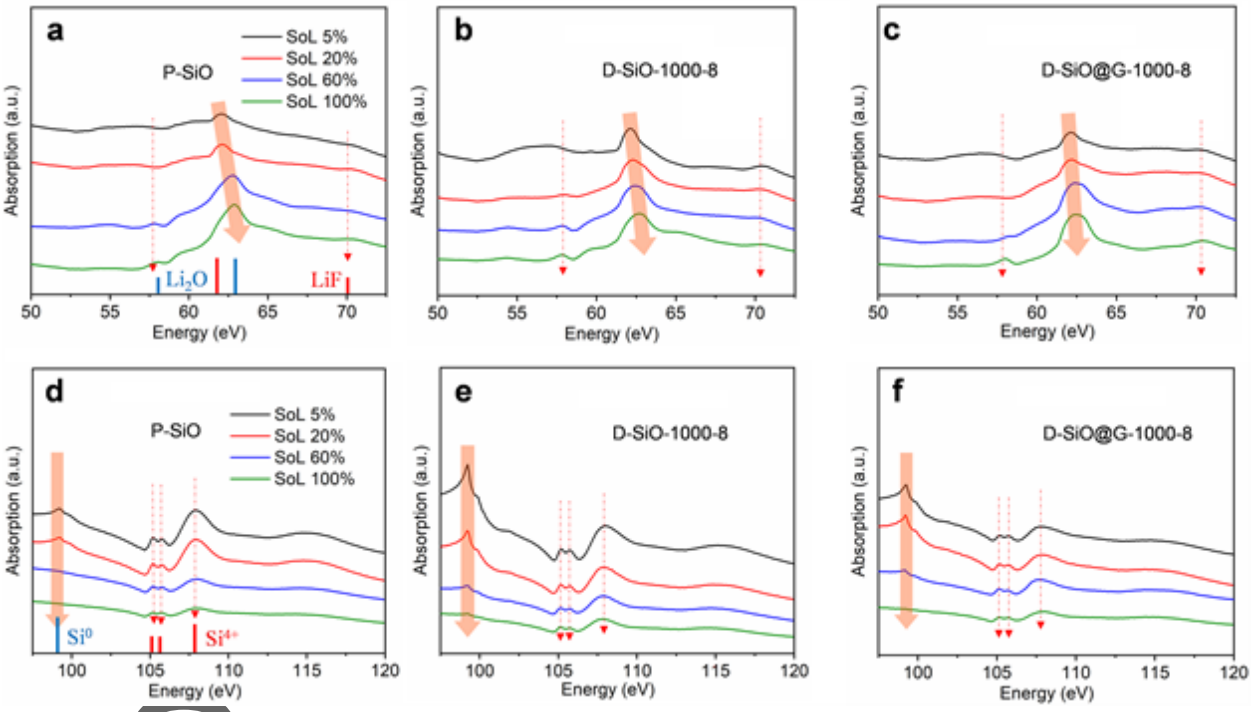

Figure 4. Li K-edge XANES spectra of (a) P-SiO, (b) D-SiO-1000-8, and (c) D-SiO@G-1000-8 electrodes at a series of SoL. Si L-edge XANES spectra of (d) P-SiO, (e) D-SiO-1000-8, and (f) D-SiO@G-1000-8 electrodes at a series of SoL.

X-ray Absorption Near-Edge Structure spectroscopy (XANES) as a powerful tool for analyzing the chemical composition and distribution of electrode interface and bulk was conducted at the VLS-PGM beamline of the Canadian Light Source. **Figures 4**a, b, and c reveal the Li-K edge XANES spectra of the P-SiO, D-SiO-1000-8, and D-SiO@G-1000-8 electrodes respectively as a function of the state of lithiation (SoL) (5%, 20%, 60%, and 100%) in the first lithiation (Figure S6). In the three graphs, three peaks can be allocated to two compounds, LiF (peaks at ~ 62 eV and ~ 70 eV) and Li_2O (~ 58 eV and ~ 63 eV), as indicated in the XANES library for lithium compounds.[32] Li_2O originates through two routes: 1) the lithiation reaction of SiO, and 2) the decomposition product of two unstable SEI

components, Li_2O_2 and Li_2CO_3, caused by the soft X-ray radiation during the XANES measurement. Route 2 is trivial and neglectable in our testing due to limited X-ray exposure time (<10 min).[14b, 32-33] The low Li-K edge excitation energy (50 eV- 75 eV) leads to an analysis depth of approximately 15 nm (Figure S7a), which is ideal for analyzing the chemical composition of the SEI film formed in the initial lithiation process. All three spectra (SoL 5%) in Figures 4a, b, and c had two peaks (~ 62 V and ~ 70 eV) in the initial discharge (lithiation) process corresponding to a lithiation potential of 0.5 V, attributable to LiF: a major characteristic component of SEI film.[14b] A new peak at ~58 eV appears with an SoL increase from 5% to 100%, accompanied by the shift of the main peak from ~ 62 eV to ~ 63 eV. The peak shift degree was in the order: P-SiO > D-SiO-1000-8 > D-SiO@G-1000-8, as indicated by the orange arrow (Figure 4a-c). With the SoL of 100%, the main peak in P-SiO had the largest shift, indicating the Li_2O overtake LiF on the particle surface, while the D-SiO@G-1000-8 peak has no apparent shift, indicating LiF remains dominant along with Li_2O. In other words, the latter has a more stable surface chemical composition. Since the analysis depth of the Li-K edge is greatly overlapped with the thickness of the SEI film formed in the initial lithiation, it is safe to conclude that the SEI film formed on the D-SiO@G-1000-8 is more stable than the other two counterparts. Combining with the initial lithiation (discharge) capacity data in Table 1, P-SiO (2564.8 mAh g^{-1}) delivered a capacity 30.3% higher than D-SiO-1000-8 (1968.9 mAh g^{-1}), we further infer that the accompanied severe volume change from the high capacity of P-SiO breaks the as-formed SEI, leaving more Li_2O in lithiated SiO exposed and then detected.[34]

Figure 4 (d, e, and f) illustrates the Si-L edge XANES spectra of the P-SiO, D-SiO-1000-8, and D-SiO@G-1000-8 electrodes with an initial SoL series of 5%, 20%, 60%, and 100%, respectively. The peaks at 99 eV in each graph are associated with Si^0, also referred to as Si nanoclusters, while those from 104 –109 eV are attributable to Si^{4+}, also referred to as the SiO_2 phase.[35] Specifically speaking, the first two peaks around 105-106 eV can assign to Si3s, while the broad peak at 108 eV is Si3d state.[36] D-SiO-1000-8 exhibits the most intense Si peak due to the disproportionation of SiO, while the Si peak for D-SiO@G-1000-8 is slightly weaker due to carbon coating. It is also visible that D-SiO@G-1000-8 has a lower Si3d state, which might reflect the Si-O-C interaction, and this is the key electronic structure observation by XANES. The detection depth of the Si L-edge XANES spectra can be 110 nm at 99 eV (Figure S7b), which is deep enough to gain the bulk information inside particles. With the increase of SoL in the initial lithiation process, Si reacts with Li-ions, forming Li_xSi alloys; while SiO_2 reacts with Li-ions, and mainly forms Li_2O and Li silicates, leading to the declination of all peaks. All three electrodes show a gradual decrease of Si3d intensity along with lithiation which might indicate that charge compensation involves Si3d state. The Si^0 peak of the P-SiO and D-SiO@G-

1000-8 electrodes disappear when the SoL reaches 100%, while the D-SiO-1000-8 electrode still has some residual. This observation indicates that some Si nanoclusters are not able to react with Li-ions in D-SiO due to the resistance of the exterior SiO_2 shell and interior SiO_2 matrix, resulting in a capacity loss. As for sample D-SiO@G-1000-8, the graphene coating limits the growth of the SiO_2 shell and makes the particles more conductive than D-SiO-1000-8, leading to a higher lithiation degree. The evolution of the surface and bulk composition revealed by the XAENS analysis agrees well with their electrochemical behaviors.

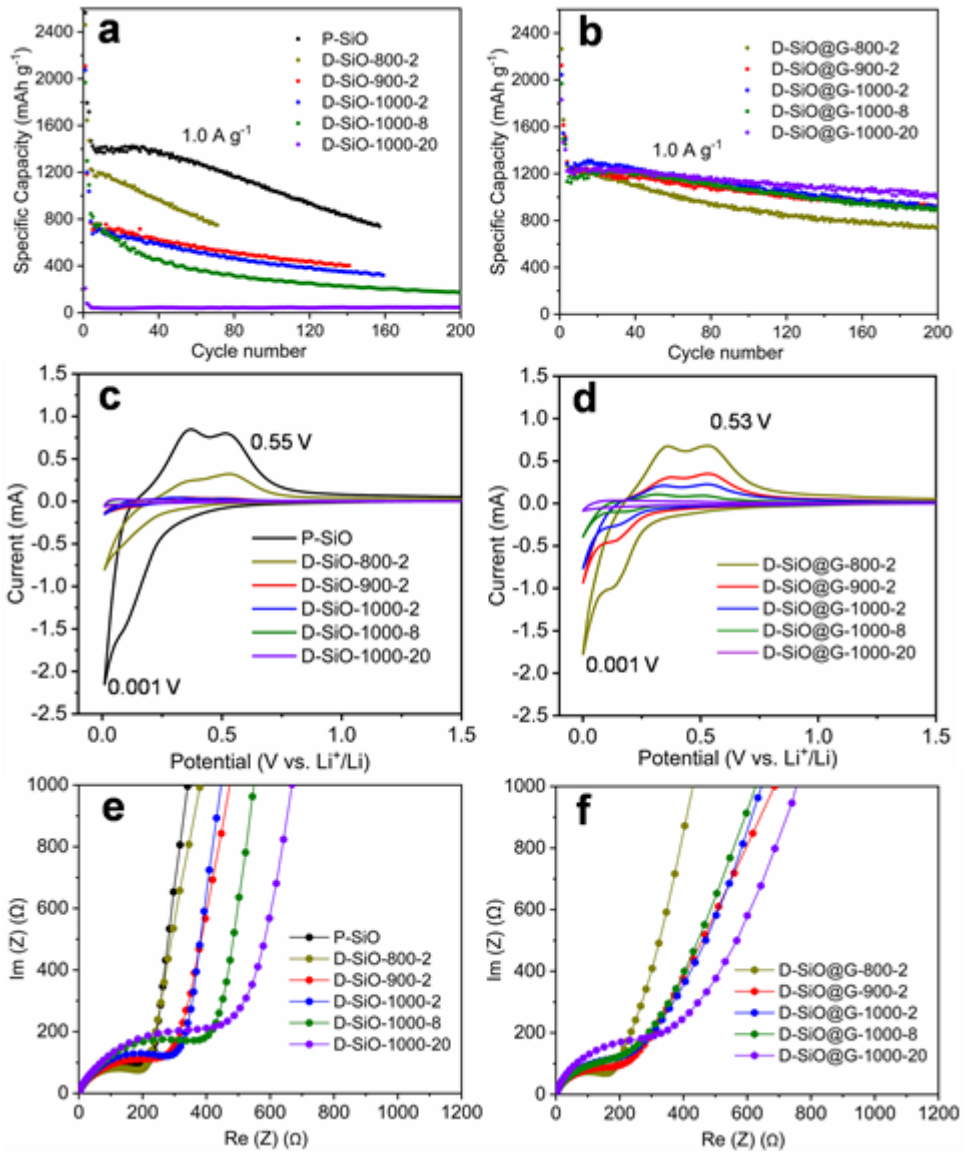

Figure 5. Cycling performance of a) SiO and b) D-SiO@G samples (50 mA g^{-1} for the first cycle, 200 mA g^{-1} for the second and third cycles, and 1,000 mA g^{-1} for the rest cycles). Cyclic voltammetry curves (third cycles) for the c) SiO and d) D-SiO@G samples. Nyquist plots of the e) SiO and f) D-SiO@G samples.

The effect of the heat treatment and carbon coating on electrochemical performance is further illustrated in **Figure 5**. P-SiO has the best cycling performance among SiO samples, delivering a reversible capacity of 1468.2 mAh g^{-1} at 1000 mA g^{-1} with a capacity retention of 51.2% after 150 cycles (Figure 5a). The cycling performance of D-SiO significantly deteriorates with an increase in heating temperature and time. The Si nanoclusters inside the D-SiO particles cannot react with Li-ions when heat-treated at 1000 °C for 20 h due to the impenetrable exterior SiO_2 shell, resulting in a limited reversible capacity of 45.6 mAh g^{-1} at 1000 mA g^{-1}. In contrast, D-SiO samples with carbon coating tend to have improved cycling performance (Figure 5b). D-SiO@G-1000-20 has the best cycling performance with a reversible capacity of 1223.2 mAh g^{-1} and capacity retention of 84.2% after 200 cycles. This improvement can be explained by two reasons: 1) the carbon coating prevents the side reactions between D-SiO particles and the electrolyte, facilitating durable cycling,[37] and 2) the heat treatment process increases the density and resistivity of the SiO_2 phase,[21] making Li-ion transport difficult, and resulting in a lower capacity accompanied by a smaller volume change during cycling, which is conducive to a longer cycling life. A capacity increase can be detected from the samples heat-treated at 1000 °C and some reports,[16] in the incipient tens of cycles (Figure 5b), which can be attributed to the additional lithiation of the unreacted SiO_2 phase and its embedded Si nanoclusters.

The cyclic voltammetry (CV) of the SiO and D-SiO@G samples was performed at a scan rate of 0.1 mV S^{-1}. The first cycle of the CV profiles for the SiO (Figure S8a) and D-SiO@G samples (Figure S8b) indicate that all anodic and cathodic currents drop significantly with the increase in heating temperature and time due to the resistance of the as-formed dense and dielectric SiO_2 phase. The values of the redox current for each sample increase in subsequent cycles as more silicon participates in the lithiation and delithiation processes.[38] In the third CV cycle, the SiO (Figure 5a) and D-SiO@G samples (Figure 5b) exhibit reduction peaks in the range of 0.001-0.2 V corresponding to the lithiation of SiO, while the oxidation peaks at 0.3-0.5 V can be attributed to the delithiation process. D-SiO@G samples have the smaller redox peak potential difference (ΔE_p: ~ 0.53 V for D-SiO@G samples and ~ 0.55 V for D-SiO samples), and larger redox currents than their corresponding D-SiO samples, indicating a faster and more intense redox reaction response due to the graphene coating. These results are also supported by the EIS results. The Nyquist plots for all SiO (Figure 5e) and D-SiO@G samples (Figure 5f) possess one depressed semicircle in the high-frequency area corresponding to charge transfer and an inclined line in the low-frequency area associated with Li-ion diffusion. The charge-transfer resistance for SiO samples increases when heat-treated at a higher temperature and longer time. The D-SiO@G samples deliver a smaller charge-transfer resistance

than the corresponding D-SiO samples for the same reason as the CV results: the graphene coating and the subsequent reduced exterior SiO_2 shell facilitate electron transfer and Li-ion transport.

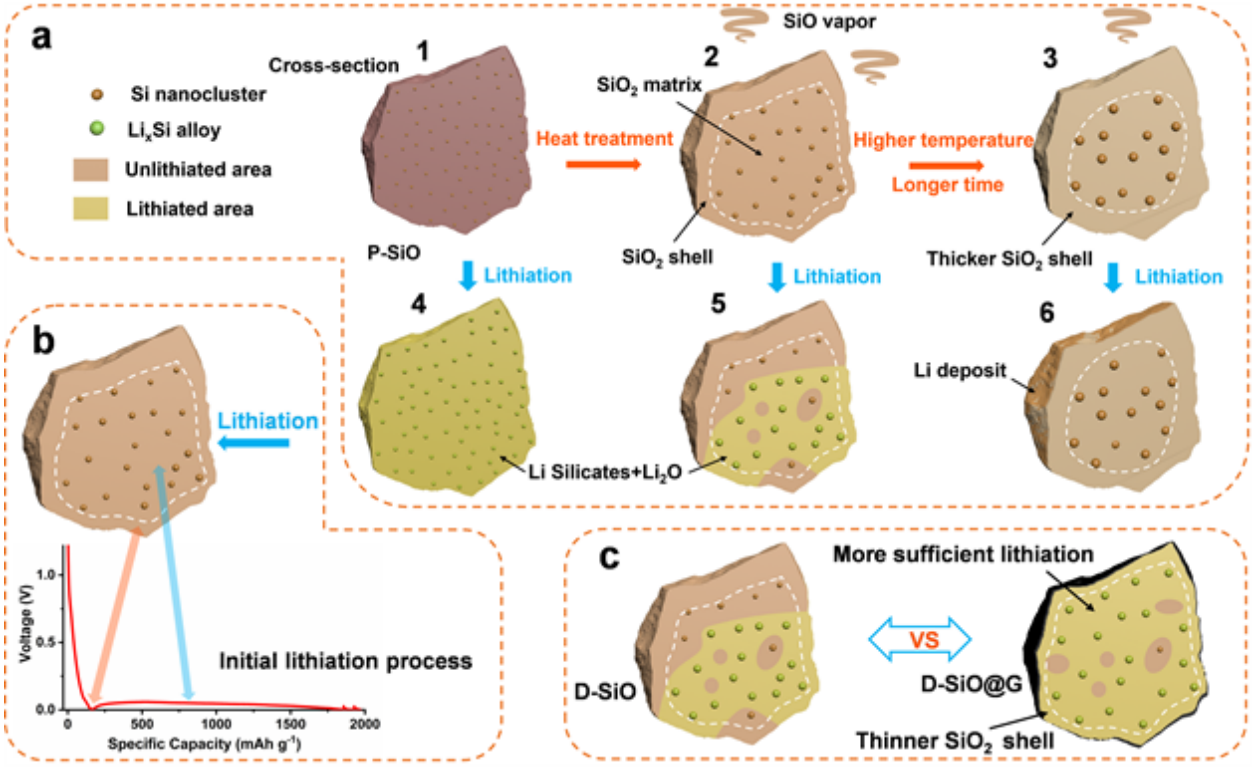

Figure 6. a) Schematic diagram of the relationship between the electrochemical behavior and the composition and microstructure of SiO induced by heat treatments. The dashed line in each particle denotes the schematic boundary between the SiO_2 shell and SiO_2 matrix. b) Schematic diagram of D-SiO materials in the initial lithiation process. c) Schematic diagram of the effect of graphene coating. The particle colors reflect the actual color change observed in the experiment. The dashed line indicates the boundary between the surface and the bulk, corresponding to the boundaries labeled in the HR-TEM image in Figure 2. The yellow section in Figures 6a4, 6a5, and 6c depict the areas where lithiation occurs effectively.

We investigated the effect of the heat treatment and carbon coating processes on SiO composition and microstructure changes and explicated the relationships between their morphology and electrochemical behaviors. Here, we propose a schematic model in **Figure 6** to establish the SiO structure evolution during the heat treatment and carbon coating processes. P-SiO has Si nanoclusters in the surrounding amorphous SiO_2 matrix, delivering considerable discharge capacity during the lithiation process (Figures 6a1→6a4). The high-temperature heat treatment applied to P-SiO (Figure 6a) triggers disproportionation (Figures 6a1→6a2), expediting the Si and SiO_2 phase separation and forming a more inert and denser SiO_2 matrix and larger Si nanoclusters. High temperature also sublimates a certain amount of SiO, generating SiO vapor, which partially deposits

onto the top of the sample powder, forming Si nanowires, while a certain proportion condensed and deposited onto the surface of the surrounding SiO particles where oxygen atoms tend to enrich outward, forming an exterior layer of SiO_2 shell (Figure 6a2). The lithiation of D-SiO (Figure 6a2→6a5) is insufficient as evidenced by the XANES analysis and the capacity loss compared with P-SiO because 1) the SiO_2 phase, including both the exterior SiO_2 shell and interior SiO_2 matrix, has a higher lithiation energy barrier and only partially participated in the lithiation reaction, and 2) the SiO_2 shell on the surface hinders the lithiation of the Si phase since Li-ions must migrate through it before reacting with the interior Si nanoclusters (Figure 6b), causing the max overpotential (Figure 6b, orange arrow). Further lithiation of the interior Si nanoclusters is also hindered by the inert and resistive interior SiO_2 matrix, resulting in decreased lithiation plateau potential (Figure 6b, blue arrow) and some unreacted areas (Figure 6a5). When treated at a higher temperature and longer time (Figure 6a2→6a3), the exterior SiO_2 shell becomes thick enough to prevent Li-ions from passing through and cause a Li-deposit onto the D-SiO surface (Figure 6a3→6a6), resulting in a significant capacity loss. The graphene coating process illustrated in Figure 6c significantly limited the growth of the exterior SiO_2 shell by confining SiO sublimation at high temperatures, facilitating the charge transfer through the surface and preventing the side-reactions between SiO and the electrolyte, leading to a thinner and more stable SEI, higher ICE, and better cycling performance.

3. Conclusion

In summary, we systematically investigated the composition and structure evolution of amorphous SiO under a series of heat and carbon coating treatments, as well as the resultant electrochemical behaviors, including the initial lithiation profiles, ICEs, and cycling life. SEM and TEM results provide direct evidence on the formation of Si nanowires, the exterior SiO_2 shell, and the interior SiO_2 matrix. Electrochemical testing and XANES analysis indicate the as-formed dielectric SiO_2 phase severely hinders the lithiation process, polarizes electrodes, subsequently causes severe overpotential, leading to capacity loss and deteriorated cycling life. While carbon coating on SiO effectively restricts the growth of the SiO_2 shell, facilitating the alloy reactions of Li-ions and the interior Si nanoclusters, accompanied by a stable SEI. As a result, a higher ICE (79.3%) and improved cyclability (84.2% after 200 cycles) are achieved. Our findings resolve some of the long-standing questions on SiO, meanwhile, offer important insights for the future design and application of SiO-based anode materials.

4. Experimental Section

D-SiO preparation: Disproportionated SiO (D-SiO) powder was prepared by sintering pristine SiO (P-SiO, D_{50} = 5 μm, the atomic ratio of Si and O = 1:1, Alibaba) using a series of heat treatment

processes (300 °C for 2 h, and then at 800 °C for 2 h, 900 °C for 2 h, 1,000 °C for 2 h, 1,000 °C for 8 h, and 1 000 °C for 20 h) with a ramp rate of 5 °C min^{-1} under a reducing atmosphere (10% H_2 with 90% Ar) in a TFM2 two-zone tube furnace (Across International, USA). The obtained D-SiO samples were named D-SiO-800-2, D-SiO-900-2, D-SiO-1000-2, D-SiO-1000-8, and D-SiO-1000-20. Another series of disproportionated SiO (D-SiO) powder was prepared using the same heat treatment process except under a pure Ar atmosphere.

D-SiO@G preparation: Humic acid, extracted and purified from North Dakota lignite according to our previous reports, was used as the carbon source in the carbon coating process.[28] Humic acid (2.5 g) and 10 g of P-SiO powder were mixed in 100 mL of DI water, then 1 mL of ammonium (28% - 30%, LabChem USA) was added dropwise into the mixture to dissolve the humic acid completely. This slurry was stirred vigorously for 1 hour then spray dried (Spray Dryer TP-S15, Toption) with an inlet temperature of 200 °C. The powder was then sintered using the same heat treatment process as the D-SiO preparation. A series of D-SiO with graphene coating composites (D-SiO@G) were obtained upon cooling to room temperature. The obtained D-SiO@G composites were named D-SiO@G-800-2, D-SiO@G-900-2, D-SiO@G-1000-2, D-SiO@G-1000-8, and D-SiO@G-1000-20.

Materials characterization: Powder X-ray diffraction (XRD) profiles were collected using an X-ray diffractometer (Smartlab, Rigaku) at an accelerating voltage of 40 kV, a tube current of 44 mA, and a scan rate of 2° min^{-1} from 10° to 80°. Field-emission transmission electron microscopy (FE-TEM, JEM-2100F, JEOL, 200 kV) and field-emission scanning electron microscopy (FE-SEM, Quanta 650 FEG, FEI) were conducted to analyze particle morphology and microstructure. X-ray photoelectron spectroscopy was conducted using a PHI 5600ci spectrometer equipped with a hemispherical electron analyzer and a monochromatic Al Kα (1486.6 eV) radiation source. A carbon analyzer (TOC-V, SHIMADZU) with an SSM 5000A module was used to calculate the carbon content of the D-SiO@G composites.

Electrochemical measurements: Active materials, conductive agent (acetylene black), CMC (Carboxymethyl Cellulose), and SBR (Styrene-Butadiene Rubber) with a mass ratio of 60:20:8:12 were mixed in DI water for 8 h to prepare the electrode paste. The paste was spread onto a copper foil and dried overnight in a vacuum at 100 °C. The coated copper foil was punched into disks with a diameter of 14 mm to create working electrodes, in company with lithium foil as the counter electrodes, 1.2 M $LiPF_6$ in EC/DMC/EMC (1/1/1 in wt%) with 10 wt% FEC as the electrolyte, and Celgard 2400 membrane as the separator to assemble CR2032 coin cells. Galvanostatic charge-discharge testing between 0.001 V and 2.0 V (vs. Li/Li$^+$) was performed with a battery testing system (CT-4008, Neware Technology Limited, Shenzhen, China) at room temperature. In this work, the

discharge process represented the lithiation process while the charge was delithiation. Cyclic voltammetry (CV) and electrochemical impedance spectroscopy (EIS) were conducted on a potentiostat (Interface 1010E, Gamry Instruments, USA).

P-SiO, D-SiO-1000-8, and D-SiO@G-1000-8 electrodes with an initial status of lithiation (SoL) were investigated with Si L-edge and Li K-edge X-ray Absorption Near-Edge Structure spectroscopy (XANES) at the VLS-PGM beamline of the Canadian Light Source, University of Saskatchewan. Electrodes in half coin cells were first lithiated to a specific state of lithiation (SoL) then disassembled and rinsed with acetonitrile (>99.5%, Fisher Chemical) in a glovebox. The electrodes were dried in an ultra-pure Ar atmosphere, attached to the sample holders under an Ar atmosphere, then transferred into the vacuum chamber of the beamline's endstation. The XANES spectra were collected and analyzed using a microchannel plate detector in the fluorescent yield mode (FLY).[39] A high vacuum ($< 1 \times 10^{-7}$ torr) was maintained in the experimental chamber during the test. The collected FLY data were normalized with the I_0 current, measured using a nickel mesh placed in front of the sample. The energy shift of the beamline was calibrated by the LiCl during the test. Please refer to the reference for detailed operation procedures.[32]

Supporting information

Supporting Information is available from the Wiley Online Library or from the author.

Acknowledgements

The Raman work was kindly supported by Jennifer Weidman, Congjun Wang, and Christopher Matranga from National Energy Technology Laboratory (NETL). The support of the United States Department of Energy, National Energy Technology Laboratory through NETL-Penn State University Coalition for Fossil Energy Research (UCFER, contract number DE-FE0026825) is greatly appreciated. The authors acknowledge the financial support from Clean Republic LLC. The authors also acknowledge support from Canadian Light Source Inc., Saskatoon, Canada. Part of the research described in this paper was performed at the Canadian Light Source, a national research facility of the University of Saskatchewan, which is supported by the Canadian Institutes of Health Research (CIHR), the Canada Foundation for Innovation (CFI), the National Research Council (NRC), the Natural Sciences and Engineering Research Council (NSERC), the Government of Saskatchewan, and the University of Saskatchewan.

Conflict of Interest

The authors declare no conflict of interest.

Received: ((will be filled in by the editorial staff))
Revised: ((will be filled in by the editorial staff))
Published online: ((will be filled in by the editorial staff))

References

[1] a) M. Armand, J.-M. Tarascon, *Nature* **2008**, *451*, 652; b) D. Ma, Z. Cao, A. Hu, *Nano-Micro Lett.* **2014**, *6*, 347.

[2] a) C.-M. Park, J.-H. Kim, H. Kim, H.-J. Sohn, *Chem. Soc. Rev.* **2010**, *39*, 3115; b) U. Kasavajjula, C. Wang, A. J. Appleby, *J. Power Sources* **2007**, *163*, 1003.

[3] A. Casimir, H. Zhang, O. Ogoke, J. C. Amine, J. Lu, G. Wu, *Nano Energy* **2016**, *27*, 359.

[4] J.-H. Kim, C.-M. Park, H. Kim, Y.-J. Kim, H.-J. Sohn, *J. Electroanal. Chem.* **2011**, *661*, 245.

[5] a) Z. Liu, Q. Yu, Y. Zhao, R. He, M. Xu, S. Feng, S. Li, L. Zhou, L. Mai, *Chem. Soc. Rev.* **2019**, *48*, 285; b) J. Yang, Y. Takeda, N. Imanishi, C. Capiglia, J. Xie, O. Yamamoto, *Solid State Ionics* **2002**, *152*, 125.

[6] J. A. Yasaitis, R. Kaplow, *J. Appl. Phys.* **1972**, *43*, 995.

[7] A. Hohl, T. Wieder, P. Van Aken, T. Weirich, G. Denninger, M. Vidal, S. Oswald, C. Deneke, J. Mayer, H. Fuess, *J. Non-Cryst. Solids* **2003**, *320*, 255.

[8] G. W. Brady, *J. Phys. Chem.* **1959**, *63*, 1119.

[9] H. R. Philipp, *J. Non-Cryst. Solids* **1972**, *8*, 627.

[10] A. Hirata, S. Kohara, T. Asada, M. Arao, C. Yogi, H. Imai, Y. Tan, T. Fujita, M. Chen, *Nat. Commun.* **2016**, *7*, 1.

[11] S. C. Jung, H.-J. Kim, J.-H. Kim, Y.-K. Han, *J. Phys. Chem. C* **2015**, *120*, 886.

[12] a) T. Tan, P.-K. Lee, Y. Denis, *J. Electrochem. Soc.* **2018**, *166*, A5210; b) C.-H. Doh, C.-W. Park, H.-M. Shin, D.-H. Kim, Y.-D. Chung, S.-I. Moon, B.-S. Jin, H.-S. Kim, A. Veluchamy, *J. Power Sources* **2008**, *179*, 367.

[13] a) I. Choi, M. J. Lee, S. M. Oh, J. J. Kim, *Electrochim. Acta* **2012**, *85*, 369; b) H. Xiao, C. Fang, T. Zheng, H. Bai, G. Liu, *APL Materials* **2022**, *10*, 011108; c) H. Xiao, T. Zheng, G. Liu, H. Wang, H. Bai, Y. Fu, Z. Tao, N. Si, H. Bai, in *IOP Conference Series: Earth and Environmental Science*, Vol. 242, IOP Publishing, Surabaya, Indonesia **2019**, 042014.

[14] a) Z. Lin, J. Li, Q. Huang, K. Xu, W. Fan, L. Yu, Q. Xia, W. Li, *J. Phys. Chem. C* **2019**, *123*, 12902; b) C. C. Nguyen, H. Choi, S.-W. Song, *J. Electrochem. Soc.* **2013**, *160*, A906.

[15] H. Li, H. Li, Z. Yang, L. Yang, J. Gong, Y. Liu, G. Wang, Z. Zheng, B. Zhong, Y. Song, *Small* **2021**, *17*, 2102641.

[16] a) L. Shi, C. Pang, S. Chen, M. Wang, K. Wang, Z. Tan, P. Gao, J. Ren, Y. Huang, H. Peng, *Nano Lett.* **2017**, *17*, 3681; b) M. Xia, Z. Zhou, Y. Su, Y. Li, Y. Wu, N. Zhou, H. Zhang, X. Xiong, *Appl. Surf. Sci.* **2019**, *467*, 298.

[17] a) Z. Liu, Y. Zhao, R. He, W. Luo, J. Meng, Q. Yu, D. Zhao, L. Zhou, L. Mai, *Energy Storage Mater.* **2019**, *19*, 299; b) Y. Ren, M. Li, *J. Power Sources* **2016**, *306*, 459.

[18] a) J. I. Lee, K. T. Lee, J. Cho, J. Kim, N. S. Choi, S. Park, *Angew. Chem.* **2012**, *124*, 2821; b) Z. Lu, N. Liu, H.-W. Lee, J. Zhao, W. Li, Y. Li, Y. Cui, *ACS nano* **2015**, *9*, 2540.

[19] S. Dorofeev, A. Ischenko, N. Kononov, G. Fetisov, *Curr Appl Phys .* **2012**, *12*, 718.

[20] a) C.-M. Park, W. Choi, Y. Hwa, J.-H. Kim, G. Jeong, H.-J. Sohn, *J. Mater. Chem.* **2010**, *20*, 4854; b) O. Feroughi, C. Sternemann, C. J. Sahle, M. Schroer, H. Sternemann, H. Conrad, A. Hohl, G. Seidler, J. Bradley, T. Fister, *Appl. Phys. Lett.* **2010**, *96*, 081912.

[21] T. Tepper, S. Berger, *Nanostruct. Mater.* **1999**, *11*, 1081.

[22] K. Yasuda, Y. Kashitani, S. Kizaki, K. Takeshita, T. Fujita, S. Shimosaki, *J. Power Sources* **2016**, *329*, 462.

[23] a) N. Wang, Y. Tang, Y. Zhang, C. Lee, I. Bello, S. Lee, *Chem. Phys. Lett.* **1999**, *299*, 237; b) C. Shen, R. Fu, H. Guo, Y. Wu, C. Fan, Y. Xia, Z. Liu, *J. Alloys Compd.* **2019**, *783*, 128.

[24] a) J. Wang, X. Wang, B. Liu, H. Lu, G. Chu, J. Liu, Y.-G. Guo, X. Yu, F. Luo, Y. Ren, *Nano Energy* **2020**, *78*, 105101; b) G. Choi, J. Kim, B. Kang, *Chem. Mater.* **2019**, *31*, 6097.

[25] a) Y. Zhang, Y. Tang, C. Lam, N. Wang, C. Lee, I. Bello, S. Lee, *J. Cryst. Growth* **2000**, *212*, 115; b) W. Dewald, C. Borschel, D. Stichtenoth, T. Niermann, C. Ronning, *J. Cryst. Growth* **2010**, *312*, 1751.

[26] R. Zhang, M. Zhao, S. Lee, *Phys. Rev. Lett.* **2004**, *93*, 095503.

[27] K. Kitada, O. Pecher, P. C. Magusin, M. F. Groh, R. S. Weatherup, C. P. Grey, *J. Am. Chem. Soc.* **2019**, *141*, 7014.

[28] S. Xu, J. Zhou, J. Wang, S. Pathiranage, N. Oncel, P. Robert Ilango, X. Zhang, M. Mann, X. Hou, *Adv. Funct. Mater.* **2021**, *31*, 2101645.

[29] Z. Long, R. Fu, J. Ji, Z. Feng, Z. Liu, *ChemNanoMat* **2020**, *6*, 1127.

[30] W. Li, R. Tang, B. Yuan, Y. Wang, T. Sun, *J. Mater. Sci.* **2020**, *55*, 6005.

[31] Y. Yao, J. Zhang, L. Xue, T. Huang, A. Yu, *J. Power Sources* **2011**, *196*, 10240.

[32] D. Wang, L. Zuin, *J. Power Sources* **2017**, *337*, 100.

[33] R. Qiao, Y.-D. Chuang, S. Yan, W. Yang, *PloS one* **2012**, *7*, e49182.

[34] Q. Li, X. Liu, X. Han, Y. Xiang, G. Zhong, J. Wang, B. Zheng, J. Zhou, Y. Yang, *ACS Appl. Mater. Interfaces* **2019**, *11*, 14066.

[35] M. Kasrai, W. Lennard, R. Brunner, G. Bancroft, J. Bardwell, K. Tan, *Appl. Surf. Sci.* **1996**, *99*, 303.

[36] J. Zhou, Y. Hu, X. Li, C. Wang, L. Zuin, *RSC Adv.* **2014**, *4*, 20226.

[37] H. Li, H. Zhou, *Chem. Commun.* **2012**, *48*, 1201.

[38] H. Tian, X. Tan, F. Xin, C. Wang, W. Han, *Nano Energy* **2015**, *11*, 490.

[39] M. Kasrai, Z. Yin, G. M. Bancroft, K. H. Tan, *J. Vac. Sci. Technol* **1993**, *11*, 2694.

The table of contents entry:

SiO is among the top candidates for next-generation lithium-ion battery anodes. Heat treatment and carbon coating are two widely-used approaches that make SiO anode succeed. The fundamental "process-microstructure-electrochemical performance" relationship is thoroughly investigated and understood. The findings offer crucial insights for the future design and application of SiO-based anode materials.

Shuai Xu, Xiaodong Hou*, Dongniu Wang, Lucia Zuin, Jigang Zhou, Yong Hou, and Michael Mann

Insights into the Effect of Heat Treatment and Carbon Coating on the Electrochemical Behaviors of SiO Anodes for Li-ion Batteries

ToC figure